RESEARCH ARTICLE
doi:10.59236/geomorphica.v2i1.49

GEOMORPHICA

Observations of the dynamics of mixed sediments on a nourished beach in a mixed-energy environment

Jorn W. Bosma * [1], **Timothy D. Price** [1], **Gerben Ruessink** [1]

[1]Department of Physical Geography, Faculty of Geosciences, Utrecht University, Utrecht, the Netherlands

Author contributions: *Conceptualization*: J. W. Bosma, T. D. Price. *Methodology, Investigation, Formal analysis, Data curation, Visualization, Writing - original draft*: J. W. Bosma. *Writing - review & editing*: B. G. Ruessink, T. D. Price, J. W. Bosma. *Supervision*: T. D. Price, B. G. Ruessink. *Funding acquisition*: T. D. Price.

Abstract Sand nourishments play a crucial role in safeguarding vulnerable urbanized coastlines in wave-dominated environments. Nowadays, nourishments are also implemented as sandy retrofits in front of hard infrastructure within mixed wave-current systems using poorly sorted sediments, where the coarse fraction is expected to minimize erosion. However, the dynamics of these mixed sediments in mixed-energy systems is poorly understood. Here, we combine hydrodynamic data and sediment samples collected from the Prins Hendrikzanddijk retrofit, Texel, the Netherlands, to demonstrate that frequent remixing of the bed (sub)surface disrupts sediment sorting processes, preventing the formation of a more erosion-resistant composition (armor layer). Despite the low-energy environment and the use of coarser-than-native sediments, tidal currents are shown to commonly mobilize the finer particles, while moderate storm waves also mobilize the coarser fractions. Additionally, the cross-shore exchange of sediments between the upper and lower beach in response to changing wave conditions further prevents long-term sorting, as this profile dynamic exposes new coarse, poorly sorted material at the surface. Our finding that a stable armor layer does not develop can lead to higher erosion rates over time than anticipated.

Non-technical summary Protecting coastlines from rising sea levels, storm waves, and strong currents often involves adding sand to vulnerable areas to act as a protective buffer. This is also done in front of hard structures such as sea walls, even in areas where sand is not naturally abundant. Mixing coarse grains with the sand can help reduce erosion, as heavier grains are less likely to wash away. Over time, under mild wave conditions, coarser grains are expected to become relatively more abundant at the surface. However, this study at a beach in Texel, the Netherlands, shows that this may not always happen. Tidal currents there move much of the sand around constantly, even in the absence of big waves. During storms, larger waves also move the heavier grains and cause sand from the upper and lower parts of the beach to blend. This frequent movement keeps the sand mixed and prevents the beach from becoming coarser and more erosion-resistant over time. Although the behavior of sand mixtures is typically not accounted for in the design of protective sand buffers, our results suggest that it may affect its long-term evolution, particularly in areas with limited natural sand.

Received:
January 01, 2025
Accepted:
June 25, 2025
Published:
August 18, 2025

[†] ***Non-english abstract available:*** *Dutch abstract is published online.*

1 Introduction

Sandy nourishments have become an increasingly popular tool for maintaining the safety of urbanized coastal beaches in the face of increasing relative sea levels and more extreme weather events (de Schipper et al., 2021). Sometimes, nourishments are implemented in front of existing hard infrastructure, for example a sea wall that needs an upgrade (e.g., Kroon et al., 2022), in which case we speak of a sandy retrofit. Nourishments are seen as an approach that fits better into the natural sandy system (de Vriend et al., 2015).

Sand is often highly dynamic and has an intrinsic tendency to disperse and disappear, especially in areas experiencing chronic erosion (de Schipper et al., 2016; Arriaga et al., 2020). That is why the sediments chosen for nourishment are usually coarser than the native bed material to reduce dispersion rates. In addition, the sediments used are sometimes extracted from multiple distant source regions. When these diverse sediments are then brought together within a single system, they can form a poorly sorted mixture.

On macrotidal coasts, coarse sand requires a relatively high combined wave-current energy for transport, while fine sand can often still be moved even during calm to moderate conditions or by (tidal) currents alone (Huisman et al., 2016). However, when fine and coarse grains are mixed together, it becomes more complicated, as detailed laboratory flume studies have demonstrated that the various fractions within a sand mixture cannot be considered independently when examining sediment pathways and morphologic changes (O'Donoghue and Wright, 2004; Hassan and Ribberink, 2005). The hiding of smaller particles and the increased exposure of larger particles alter their respective critical shear stresses required for mobilization (Egiazaroff, 1965; Vollmer and Kleinhans, 2008), thus changing the

*Corresponding author: j.w.bosma@uu.nl

expected behavior of the mixture.

Sorting mechanisms are thought to play an important role in the rate and manner in which the sand is transported. These mechanisms can alter the grain size fractions that are directly exposed at the bed surface and thus subjected to hydrodynamic forces, while also reshaping the grain size composition of the subsurface layers. Consequently, this vertical sorting modifies the hiding-exposure effects that regulate sediment mobility and entrainment (Kleinhans, 2005b) and, in combination with lateral sediment transport, may lead to spatial sorting patterns both cross- and alongshore. Despite the clear implications for sediment dynamics and morphological development, spatial heterogeneity in grain sizes is still rarely taken into account in morphologic studies of coastal interventions.

Much effort has been put into developing a generic sediment transport model that accounts for non-uniform sand mixtures. Egiazaroff (1965) introduced a type of hiding-exposure (HE) function in the calculation of the critical bed shear stress (BSS) based on the grain size fraction of interest (D_i) relative to the median (D_{50}). Many adaptations have since followed with varying performance, most of which focused on fine-tuning the calibration coefficients through empirical testing (Ashida and Michiue, 1973; Hayashi et al., 1980; Parker et al., 1982; Wilcock and Crowe, 2003; McCarron et al., 2019). Moreover, dynamic poorly sorted surface layers are even more challenging, as they constantly change surface composition and, with it, the HE function itself.

In addition to bed composition, the hydrodynamic boundary conditions and the initial morphology of a sand body also steer the transport rate and manner (Arriaga et al., 2020). Most previous morphodynamic studies have focused on open-coast systems dominated by swell or high-energy storm waves (e.g., Huisman et al., 2018; Townsend et al., 2024). On such coasts, particularly sandy beaches, the thresholds for incipient motion are often exceeded for all grain sizes during some portion of the wave cycle. By contrast, protected systems within tidal basins tend to hover around threshold conditions. Tidal basins are mixed-energy environments often characterized by strong tidal currents and locally generated low-energy waves, which together account for sediment transport and beach morphodynamics (e.g., Blackley and Heathershaw, 1982; Vila-Concejo et al., 2010; Elias et al., 2012; Vila-Concejo et al., 2024). In addition, the morphology at such sheltered sites may differ considerably from that at wave-dominated coasts, often containing deep tidal channels and shallow shoals (Vila-Concejo et al., 2024). Beaches in tidal basins often have a compound cross-shore profile consisting of a steep upper 'surf' part and a lower 'shoaling' part (Hegge et al., 1996; Bernabeu et al., 2003; Travers et al., 2010; Nordstrom and Jackson, 2012). These differences in hydrodynamic forcing, sediment threshold exceedance and beach morphology raise the question of whether previous findings from open coasts can be projected onto sheltered coasts. What role do sediment sorting processes play here?

The current lack of a generic and accurate deterministic model for predicting mixed-sediment transport underscores the need for extensive field observations in various coastal systems with different wave-current dominance and energy level, extending well beyond laboratory scales. The literature on this subject is particularly sparse on large-scale interventions in mixed-energy environments, especially when the introduced sediments differ significantly from the native bed material, resulting in a poorly sorted mixture. Therefore, it has become increasingly important to understand how bed composition evolves when non-native sediment sizes are introduced into a system. Here, we capitalize on a recent sandy retrofit project in the Netherlands, which serves as an ideal case study due to its sheltered location within a tidal basin and its complex sediment composition. The objective of this paper is to evaluate grain size dispersion in relation to the dynamics in wave and tidal forcing as well as beach morphology. This will be achieved by analyses of a combination of sediment samples from the beach face, computations of BSS and sediment transport rates, and changes in bed elevation.

2 Study Site

The Prins Hendrikzanddijk (PHZ), which translates to "Prince Hendrik Sand Dike" in English, is a sandy retrofit located on the Wadden Sea (basin) side (southeast) of Texel, the westernmost barrier island of the Netherlands (Fig. 1). Along the Texel coast, several traditional dike segments, including the Prins Hendrikdijk, failed to meet the updated safety standards introduced in the revised Dutch Water Act (Fordeyn et al., 2019). To address this issue, the original concrete dike (length ≈ 3 km) was refurbished in 2019. This refurbishment involved the construction of a large sand body placed on top of the shallow subtidal platform, the Schanserwaard (NAP-0.8 to -2.2 m; Dutch Ordnance Datum, where NAP+0 m is equivalent to mean sea level), with the aim of fully taking over the function of primary flood defense.

Its design comprises a high foredune with a crest elevation of approximately NAP+8 m, fully planted with European marram grass, a low-lying beach area to the south (slope ≈ 1:13) and a spit toward the northeast (slope ≈ 1:6–8). The spit crest sits at approximately NAP+3 m and, together with the roughly parallel foredune strip, partially encloses a shallow lagoon. On the seaward side, the intertidal beach is narrow (width ≈ 25 m) and separated from the dry beach (width ≈ 100 m) by a scarp line (height ≈ 0.1 m). The two primary orientations of the coastline are 46°N and 42°N (clockwise rotation) along the spit and the southern beach, respectively, enabling a large fetch for the dominant southwesterly winds. At the proximal end of the spit and close to the dividing point between these two coastline orientations, a miniature tombolo-like shape (several meters across) protrudes from the beach onto the platform. To the west of the nourishment, a harbor jetty shields the adjacent part of the beach from southerly waves and currents, creating a sheltered corner (Fig. 1).

The area has a semi-diurnal tide with a mean (spring) tidal range on the basin side of the inlet of approx-

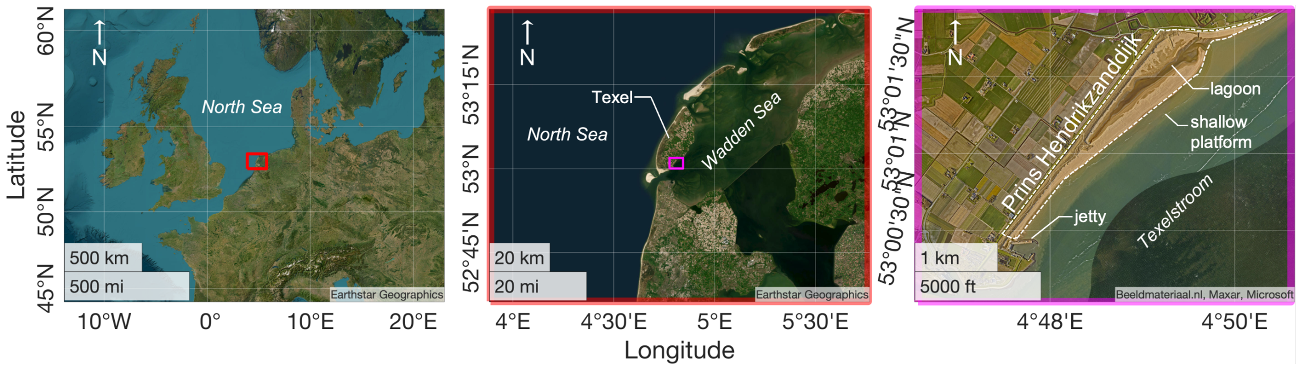

Figure 1 Location of the Prins Hendrikzanddijk, a sandy retrofit at the southeast side of the barrier island of Texel, the Netherlands.

imately 1.4 m (2 m) (Elias et al., 2006). The flood-dominant tide enters and leaves through the Marsdiep tidal inlet and travels through the Texelstroom, a 20 m to 30 m-deep tidal channel (Fig. 1). Tidal currents are relatively strong due to tidal contraction in the narrow strait with flow velocities that reach 1.8 ms^{-1} inside the inlet (Buijsman and Ridderinkhof, 2007) and up to 0.6 ms^{-1} on the subtidal platform (Brand, 2016). Due to its position within the tidal basin, waves from the North Sea cannot reach the PHZ shoreline. Therefore, the wave climate in front of the sand dike is relatively mild. Model results by Perk et al. (2019) showed the significant wave height H_{m0} to range from 0.2 m to 0.4 m with the wave period T in the range of 3 s to 5 s, with the largest waves (up to 1.4 m) arriving from the southwest, as opposed to the North Sea basin (H_{m0} = 1.3 m with T = 6 s and $H_{m0,\text{storm}}$ > 6 m; Elias et al., 2006). The maximum near-bed orbital velocities measured on the platform (pre-construction) were 0.5 ms^{-1} (Brand, 2016). As a consequence, both waves and tides are important in shaping the area's morphology, producing mixed-energy conditions.

Before the construction of the sand dike, the underlying subtidal platform consisted of fine to medium sand with a median grain size D_{50} of 0.2 mm (Brand, 2016). For the core of the sandy reinforcement, similar grain sizes were used. However, to minimize erosion and therefore future maintenance, coarse sediments were also incorporated into the design (Fordeyn et al., 2019). An approximately 1-m thick protective wear layer, composed of the coarsest fractions (> 0.4 mm), was placed on the seaward slope of the beach, with the exception of the southernmost part, which needed to remain fine to support benthos habitats. In addition, layers of shells were added on top of the beach area to create favorable bird habitat and reduce sand drift. These sediments, sourced from various extraction sites, together resulted in a highly heterogeneous mixture (e.g., Fig. 2).

3 Methods and Data

3.1 Data collection

The data analyzed in this study were collected during the 5-week SEDMEX field campaign (mixed SEDiment in Mixed Energy eXperiment; Van der Lugt et al., 2024), conducted from 9 September to 19 October 2021, about 2 years after the implementation of the nourishment. The complete dataset comprises multiple sediment sample series collected along the beach face (Fig. 4a in Van der Lugt et al., 2024) on different days and a more consistent set of cross-shore sediment samples with higher spatial and temporal resolution at one longshore location (Fig. 4b in Van der Lugt et al., 2024). In addition, bed level measurements were recorded along the same profile (transect #1 in Fig. 2 in Van der Lugt et al., 2024), and high-frequency hydrodynamic data were gathered at six longshore locations (Fig. 2 in Van der Lugt et al., 2024, excl. transect #3). Together, these observations provide detailed insights into the spatiotemporal variability of sediment composition, hydrodynamic forcing alongshore, and associated changes in beach profile. The most recent major storm to impact the study site occurred in February 2020, as reported by the Royal Netherlands Meteorological Institute (Koninklijk Nederlands Meteorologisch Instituut), well in advance of the field campaign. In addition, water level records from the official monitoring station in Oudeschild, approximately 3 km northeast of the PHZ, indicate no significant storm surge events in the months preceding the fieldwork. This is consistent with the typical seasonal pattern in the Netherlands, where the storm season normally runs from October to April. We therefore concluded that the antecedent conditions at the site were representative of a typical low-energy summer period.

3.1.1 Sediment samples

Sediment samples of 5 cm into the bed were collected at various spatial and time intervals. This sample depth was chosen as a compromise between the desired high number of samples and feasibility in subsequent processing, and was also assumed to reasonably well represent the active layer exposed to and interacting with the flow. Seven longshore locations (Fig. 3a, yellow triangles) were sampled multiple times along the NAP-0.8-m isobath, corresponding to the depth of the longshore ADV array. This alignment enabled direct association between measured flow characteristics and local bed properties. Additional samples were collected simultaneously along the NAP+0-m isobath. The cross-shore spatiotemporal variation of the bed composition in the lower part of the swash zone (from NAP+0.1 m down to about NAP-1.2 m) was captured by a series of successive sampling surveys along transect L2 (Fig. 3a) over the course of one month. At each of the eight fixed cross-shore locations (labeled S1 to S8), surface sedi-

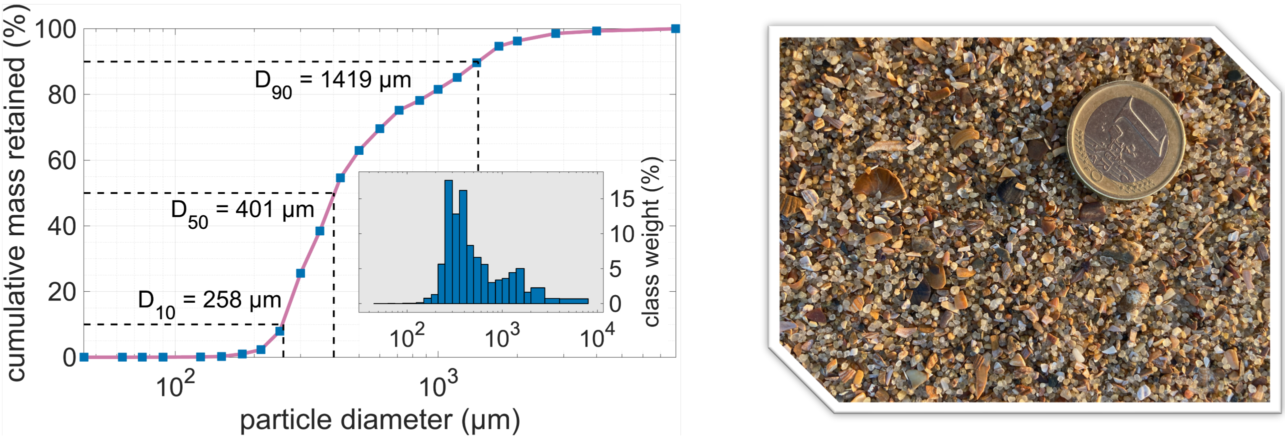

Figure 2 Example of a sediment sample collected from the top layer of the sand spit at NAP+1.6 m on 2 December 2020. The distinct modi in the frequency distribution of grain sizes and large deviation in the value of the 90th percentile are clear indicators of an additional coarse end members. CO_3 (i.e., shell) content was 10%, both by volume and mass. The 1 euro coin in the right panel has a diameter of 23.25 mm.

ment samples were collected during four phases of the tide: (1) high tide, (2) mid ebb, (3) low tide and (4) mid flood. In addition, on the 7th (spring tide) and 15th of October 2021, thin 2–6-mm layer surface samples were collected with a dedicated sand scraper device (van IJzendoorn et al., 2023) to obtain insights into the potential vertical structure and intravariation of the bulk samples. Table 1 provides an overview of the dates, locations, and number of sediment samples collected during the SEDMEX field campaign and used in this study.

Following collection, the samples were dried, mechanically sieved, and weighed. The sieving was carried out using a stacked tower of 13 sieves with mesh sizes arranged according to the Krumbein phi (ϕ) scale, with ϕ values of [-4, -3, -2.5, -2, -1.75, -1.5, -1.25, -1, -0.5, 0, 1, 2, 3]. This range corresponds to mesh widths from 63 μm up to and including 8000 μm, with a residual pan that collects finer particles. The acquired mass distributions were further processed using the open-access GRADISTAT software (Blott and Pye, 2001). Grain size statistics were calculated with the commonly used geometric (modified) Folk and Ward (1957) graphical measures:

$$M_G = \exp\left(\frac{\ln D_{16} + \ln D_{50} + \ln D_{84}}{3}\right), \quad (1)$$

$$\sigma_G = \exp\left(\frac{\ln D_{16} - \ln D_{84}}{4} + \frac{\ln D_5 - \ln D_{95}}{6.6}\right), \quad (2)$$

where M_G and σ_G are the graphic mean grain size and graphic standard deviation (i.e., sorting coefficient: the degree of uniformity), respectively, and D_i is the i^{th} percentile of the cumulative grain size distribution by mass. In the following, M_G and σ_G will always refer to these textural statistics. According to the characterization by Folk and Ward (1957), sediments are considered poorly sorted when $\sigma_G \geq 2$. Fine sand beaches along the Holland Coast typically have much lower σ_G values, indicating better sorting, whereas sand-gravel beaches often have much higher values, reflecting poorer sorting. Additional grain size metrics returning in this paper are the 10th, 50th (i.e., median) and 90th grain size percentiles derived from the local grain size distributions, and two 'global' size fractions: 0.25 mm (fine) and 2.00 mm (coarse).

To maintain an accurate representation of the bed surface at the study site, no shells were removed from the samples prior to grain size analysis. Examining the naturally mixed biogenic and non-biogenic fractions allowed for a holistic analysis of sediment sorting in relation to morphologic changes. The densities of the siliciclastic and carbonate particles at the study site were not measured directly. However, a flume study (Haarbosch, 2023) using typical North Sea sand and shells found their densities to be quite similar (2600–2800 kgm^{-3}). Based on this, we assumed equal densities for both particle types in our analysis. To quantify the possible effects on grain size metrics caused by shell valves and fragments, a follow-up analysis was applied to four random sediment samples representative of different beach sections. The subsamples were first divided into a sand and a gravel fraction using a 2-mm sieve. Their masses and dry and wet (i.e., excluding porosity) volumes were carefully determined before and after chemical removal of carbonates using a 5% HCl solution (i.e., diluted hydrochloric acid). The measured decrease in mass and volume after treatment directly reflected the shell mass and volume in the original subsamples, as the possible simultaneous dissolution of other minerals such as iron was considered minor.

Preliminary visual observations suggested large grain size gradients on the beach surface and prompted testing of the proposed sampling strategy to avoid future misidentification of large-scale patterns as artifacts of localized variability. The potential sampling error introduced by short-distance horizontal variability was quantified by comparing a series of surface samples collected within a one-meter radius. Additionally, the sand scraper samples were examined to demonstrate the significance of any vertical grading or layering and its potential impact on the derived grain size statistics of a sample.

Table 1 Overview and description of the samples and sample types. Note that the total number of samples may differ from the product of the number of dates and heights due to occasional missing or additional samples.

prefix	description	locations	day/month in 2021	heights	# samples
L	longshore	Lgn, L0, L2, L3.5, L4, Tmb, L6	21,28/9; 3,8/10	NAP+0 m & -0.8 m	41
S	cross-shore	S1–8	20,28/9; 1,7,15/10	NAP+0.2 m to -1.0 m	40
A	sand scraper	A1–3	07/10 (spring tide)	0 to -50 mm (10)	30
B	sand scraper	B1–3, Bar, Run(nel)	15/10 (neap tide)	0 to -50 mm (10)	48

3.1.2 Hydrodynamics

Waves and currents were measured along the southern beach and spit of the PHZ at six locations L1–L6 (Fig. 3a), using acoustic Doppler velocimeters (ADVs) equipped with pressure sensors. All ADVs but the one at L2, were of type Nortek Vector and sampled at a rate of 16 Hz with the measurement volume initially positioned 15 cm above the bed at NAP-0.8m. The ADV at L2 was of type SonTek ADV Ocean-Hydra and sampled at a rate of 10 Hz. An additional Nortek Vector-type ADV was deployed in deeper water (NAP-1.4m) at L2 to avoid surfacing during low tide and to allow uninterrupted time series collection (Fig. 4). All ADVs were downward-looking and measured in burst mode with a burst length of 30 min. Instrument heights were adjusted several times throughout the campaign after bed level changes to maintain the target measurement height. The processing of the recorded pressure and velocity data is described in Van der Lugt et al. (2024) and is not reiterated here. All flow properties used in the following were time-averaged over 10-minute intervals. To address uncertainties in the SonTek ADV Ocean-Hydra pressure recordings, wave height values were substituted with interpolated values derived from the two closest pressure sensors on either side of the ADV within the same cross-shore instrument array, deployed at depths NAP-0.5 m and -1.2 m.

Fig. 4 provides an overview of the conditions observed during the SEDMEX campaign. For most of the campaign, the sea remained relatively calm, except for a more energetic phase midway, characterized by significantly increased wave heights that frequently exceeded the threshold of $\mu + 2\sigma = 0.38$ m. This energetic phase, henceforth referred to as 'the stormy period', lasted roughly from 27 September to 6 October 2021. Within this period, a particularly intense interval occurred from 30 September to 3 October 2021 during which wave heights exceeded the threshold for more than half of the time.

3.1.3 Bed levels

Area-wide topography and bathymetry measurements from 2 March 2022 were provided by Jan De Nul NV, a Belgian marine construction and dredging company contracted for the PHZ project. The topography was obtained through photogrammetry from a drone (UAV) survey and the bathymetry using a vessel-mounted single-beam echosounder. The collected bed level data were processed into digital elevation models (DEMs) with a resolution of 1 m. In addition, cross-shore profile measurements were obtained roughly every other day by walking with a wheel-mounted RTK-GNSS receiver (continuous mode: 1 Hz) across the spit in line with L2 (Fig. 3a). The profiles extended approximately from the highest point on the upper beach to halfway down the subtidal platform at approximately NAP-1.5 m.

3.2 Data analysis

3.2.1 Bed shear stress

The measured hydrodynamics were translated to the different components of the dimensional and non-dimensional BSS. The grain Shields number was computed for different grain size classes:

$$\theta'_i = \frac{\tau'}{(\rho_s - \rho) \cdot g \cdot D_i}, \tag{3}$$

where τ' is the dimensional grain BSS, ρ_s is the density of the sediment, ρ is the density of the fluid, g is the acceleration due to gravity, and D_i is a characteristic particle diameter of size class i. The densities of sediment (2650 kgm^{-3}) and seawater (1025 kgm^{-3}) were assumed to be constant throughout the measuring campaign.

Unless specified otherwise, τ' refers to the total grain BSS under combined current-wave action, calculated following Soulsby and Clarke (2005), adapted from Grant and Madsen (1979):

$$\tau_{cw} = \sqrt{(\tau_w + \tau_c\,|\cos\phi_{cw}|\,)^2 + (\tau_c\,|\sin\phi_{cw}|\,)^2}, \tag{4}$$

where ϕ_{cw} is the angle between the propagation directions of the current and waves. The current component (τ_c) was computed as:

$$\tau_c = \rho \cdot g \cdot \frac{\tilde{U}^2}{C^2}, \tag{5}$$

where $\tilde{U}$ is the (time-and depth-averaged) measured current velocity determined from the law of the wall for rough flow:

$$U_z = \frac{U_*}{\kappa} \cdot \ln\left(\frac{z}{0.033 k_{s,\text{tot}}}\right), \tag{6}$$

where U_z is the velocity at level z, U_* is the shear velocity, κ is the von Kármán constant (= 0.4), and $k_{s,\text{total}}$ is the Nikuradse total (i.e., grain- plus form-related) bed roughness, here estimated as 0.05 m. The depth-averaged flow velocity can be found at $z \approx 0.368h$, where h is the water depth. The Chézy grain coefficient C is given by the White-Colebrook formula:

$$C = 18 \cdot \log_{10}\left(\frac{12h}{k_{s,\text{grain}}}\right), \tag{7}$$

where $k_{s,\text{grain}}$ is the Nikuradse grain roughness, here set equal to $2.5 \times D_{50}$ (the 50th percentile, or median, of the cumulative grain size distribution by mass). Sometimes $1 \times D_{90}$ is chosen instead, but due to the much higher representation of shell material in the coarse tails of the distributions, a multiple of the median was deemed more appropriate.

The BSS component due to waves (τ_w) is given by:

$$\tau_w = \frac{1}{2} \cdot \rho \cdot f_w \cdot U_{\text{rms}}^2, \quad (8)$$

where U_{rms} is the root-mean-square orbital velocity amplitude, computed from the orthogonal root-mean-square long- (u) and cross-shore (v) velocity components as $U_{\text{rms}} = \sqrt{2}(u_{\text{rms}}^2 + v_{\text{rms}}^2)^{1/2}$.

The wave friction factor f_w was estimated using Swart (1974) for hydrodynamically rough flow:

$$f_w = \exp\left(5.213 \left(\frac{A_{\text{rms}}}{k_{s,\text{grain}}} \right)^{-0.194} - 5.977 \right), \quad (9)$$

where A_{rms} is the near-bed orbital excursion amplitude (m) computed as:

$$A_{\text{rms}} = \frac{U_{\text{rms}}}{\omega_{\text{rms}}}. \quad (10)$$

Here, ω_{rms} is the angular frequency calculated as:

$$\omega_{\text{rms}} = \frac{2\pi}{T_{\text{rms}}}, \quad (11)$$

where T_{rms} is the root-mean-square wave period.

3.2.2 Sediment Mobility

In general, for coarse sands larger than 0.3 mm, sediment transport is primarily as bedload, with suspended transport occurring only under extreme wave and current conditions. For gravel-sized particles (> 2 mm), transport occurs almost exclusively as bedload (Soulsby and Clarke, 2005). Since the PHZ sediments are primarily larger than 0.3 mm (e.g., Fig. 2) only bedload is considered in this study. However, it should be noted that total transport during high-energy events may be underestimated if suspended load is not considered (Huisman et al., 2018).

In bedload transport studies, two important dimensionless parameters are often used: the Bonneville (1963) dimensionless grain parameter (D^*) and the critical Shields parameter (θ_{cr}). The Bonneville dimensionless grain parameter is given by:

$$D^* = D_{50} \cdot \sqrt[3]{\frac{(s-1) \cdot g}{\nu^2}}, \quad (12)$$

where s is the particle specific gravity, and ν is the kinematic viscosity of the fluid. The critical Shields number is then given by Soulsby (1997):

$$\theta_{cr} = \frac{0.30}{1 + 1.2D_*} + 0.055 \cdot [1 - \exp(-0.020D_*)]. \quad (13)$$

The critical non-dimensional shear stress for each size class is corrected with an Hiding Exposure (HE) function:

$$\theta_{cr,i,\text{corrected}} = \xi_i \cdot \theta_{cr,D_{50}}, \quad (14)$$

where ξ_i is defined as:

$$\xi_i = \left(\frac{D_i}{D_{50}} \right)^{\gamma}. \quad (15)$$

The exponent γ was set as in McCarron et al. (2019) for medium sand to fine gravel and bi-modal distributions:

$$\gamma \;= \gamma_s + (\gamma_g - \gamma_s) \cdot f_g^{1.73}, \quad (16)$$

where $\gamma_s = 0.68$ is the exponent for pure sand and $\gamma_g = 0.86$ for pure gravel, and f_g is the fraction of gravel.

The non-dimensional bedload transport predictor of Ribberink (1998) was used here, as it was carefully calibrated on large amounts of data of sand and gravel transport in combined flow with current and waves, most representative of the conditions in this study:

$$\phi_{b,i} = \alpha \cdot (\theta_i' - \theta_{cr,i})^{1.65}, \quad (17)$$

where $\alpha = 11$. This bedload transport predictor was then dimensionalized using:

$$q_{b,i} = \phi_{b,i} \cdot \sqrt{\frac{\rho_s - \rho}{\rho} \cdot g \cdot D_i^{\frac{3}{2}}}, \quad (18)$$

where $q_{b,i}$ has units m^3s^{-1} per meter width (or m^2s^{-1}). Since the focus in this study was primarily on transport in the longshore direction, while the bedload predictors were based on the total velocity vector, the predictors were corrected for the relative magnitude of the longshore velocity component:

$$q_{b,\text{long},i,\text{gross}} = q_{b,i} \cdot \frac{U_{\text{long}}^2}{U_{\text{long}}^2 + U_{\text{cross}}^2}, \quad (19)$$

where U_{long} and U_{cross} are the orthogonal long- and cross-shore velocity vectors (ms^{-1}), respectively. To incorporate the longshore direction, the gross transport rates were multiplied by the sign of the longshore current at each time step, restoring directional information:

$$q_{b,\text{long},i,\text{net}} = q_{b,\text{long},i,\text{gross}} \cdot sign\left(U_{\text{long}}\right), \quad (20)$$

where $q_{b,\text{long},i,\text{net}}$ is the net longshore transport rate, with positive values indicating transport in the flood current direction and negative values corresponding to transport in the ebb current direction. Finally, the time series of transport rates were integrated over the campaign duration to compute the total transport volumes:

$$Q_{b,i} = \int_{t_0}^{t} q_{b,i}\, dt, \quad (21)$$

where $Q_{b,i}$ has units m^3 per meter width (m^2). For net longshore transport volumes, the integration was performed separately over the positive or negative values. For the sake of comparison, time steps during which one or more ADVs were not operational were excluded from the volume calculations.

To compute bed roughness, BSS and (critical) Shields numbers along the longshore ADV array, the grain size statistics at each sampling location were averaged across the first two complete sediment surveys

(21 and 28 September 2021) and both isobaths. Bed-composition data from the sampling location closest to each ADV station were paired with the corresponding in-situ flow measurements. The specific hydrodynamic and sediment data pairings are listed in Table S1 of the Supplementary Materials.

4 Results

This section begins with an overview of the longshore variability in waves and currents along the PHZ (Sec. 4.1). It then delves into the longshore variability in grain sizes and hydrodynamic forcing (Sec. 4.3), while briefly addressing potential sediment sampling errors (Sec. 4.2). Finally, the section examines the temporal cross-shore variability in grain sizes in relation to morphologic change (Sec. 4.4).

4.1 Hydrodynamic conditions

The measured currents along the PHZ beach face exhibited considerable variability in both magnitude and direction (Fig. 3b). Generally, higher peak flow velocities were recorded toward the distal end of the spit (L1), reaching up to 0.9 ms^{-1}. The strongest currents came from the southwest, indicating a marked flood dominance. However, a deviation in this pattern was observed several hundred meters southwest at L2, where the flood currents were less pronounced. In contrast, ebb currents appeared to be somewhat dominant only in the region near the harbor jetty (south of L5), where flow velocities remained relatively low throughout the tidal cycle ($\tilde{U}_{\max}$ < 0.3 ms^{-1}). The observed dominant current directions accurately reflect the expected horizontal tide, the direction of which is strongly determined by the shape of the coastline (Figs. 3a–b). Furthermore, the magnitude of the cross-shore flow component was generally relatively small, averaging just 16% of the orthogonal longshore component on the lower beach face (Fig. 3b) and even less than 3% near the offshore platform edge (Fig. 4c).

The measured waves predominantly approached from the south to southeast (Fig. 3c and 4b), arriving at slightly oblique angles — averaging about 30° from the shore normal — along the longshore array of measurement stations (Fig. 3c). On average, the wave heights were 27% lower on the southern beach (L5–L6) compared to the spit (L1–L4), with this difference increasing to 32% during the stormy period from 27 September to 6 October 2021. Despite this, wave heights remained generally low, with a campaign-mean significant wave height of $\overline{H}_{m0}$ = 0.15 m (Fig. 4a).

4.2 Sediment sampling tests

Tests of the sediment sampling method revealed a mean horizontal sampling error of ± 143 µm for grain size, corresponding to 16% of M_G averaged across the test samples. For sample uniformity, the error was 0.29, equivalent to ± 11% of the mean σ_G. Furthermore, analysis of the eight sand scraper sample collections taken from the top 5 cm of the bed (i.e., the regular sampling depth range) revealed a mean standard deviation in grain size of 259 µm, representing 26% of the mean M_G (Fig. 5a), while the sorting coefficient showed a mean standard deviation of 0.28, or 12% of the mean σ_G (Fig. 5b). In addition, the sample-carbonate analyses indicated a mean carbonate content of approximately 16% both by mass and volume. For grain size fractions ≤ 2 mm, this value decreased to about 11%, whereas for fractions > 2 mm, it increased substantially to about 50%. These findings suggest that while shells and shell fragments introduce minimal measurement uncertainty in the bulk of the grain size distributions, their influence in the coarse ends of the spectra cannot be completely disregarded.

4.3 Longshore grain size variability

4.3.1 Grain sizes

Observations of bed surface composition along the PHZ beach face revealed significant longshore variability (Fig. 6). Despite the potential sampling biases described above, a selection of grain size distributions from the first longshore sediment sampling survey (Fig. 3d) shows that along the -0.8 m isobath, finer sediments (< 0.4 mm) were considerably more abundant at the lateral edges of the beach (L0 and L6) than in the central region (L2 and L4). Meanwhile, surface compositions along the zero isobath were more comparable to each other, although the distributions were generally wide and non-uniform in themselves (Fig. 3d).

A more detailed overview of M_G and σ_G of the surface sediment at the seven longshore sample locations in Fig. 3a, along the two isobaths, is presented in Fig. 6 using heat maps. Significant spatiotemporal differences are evident in the values of both M_G and σ_G, particularly along the lower isobath. For example, the coarsest sample (L4), collected on 28 September 2021, was nearly seven times coarser than the finest contemporary sample (L6). The sorting coefficient also varied substantially, ranging from well sorted in L6 (σ_G = 1.4) to poorly sorted in L0 (σ_G = 3.1). Data from these longshore sediment surveys indicate that the differences in M_G could be up to 170 µm over 100 m of longshore distance. However, visual observations suggest that these differences may have already occurred over much shorter distances ($\mathcal{O}(1m)$) in some areas.

The line plots in Fig. 6 visualize the overall trends depicted in the heat maps. Overall, grain sizes were larger at the lower (-0.8 m) isobath, except for the two southernmost locations (Tmb–L6). Both isobaths show a peak in M_G around the central part of the spit (L2–L4), with finer sediments toward the lateral edges. However, the differences along the lower isobath were much more pronounced, as reflected by the larger scale used for the horizontal axis. Despite the similar trends between the two isobaths, the error bars highlight significant temporal variability at most longshore locations, particularly at greater depths (except for locations Lgn, Tmb, and L6). This suggests strong temporal changes in longshore differences over time.

Most of the samples collected along the upper (87%) and lower (68%) isobaths were poorly sorted (σ_G ≥ 2). However, in some instances, samples were moderately

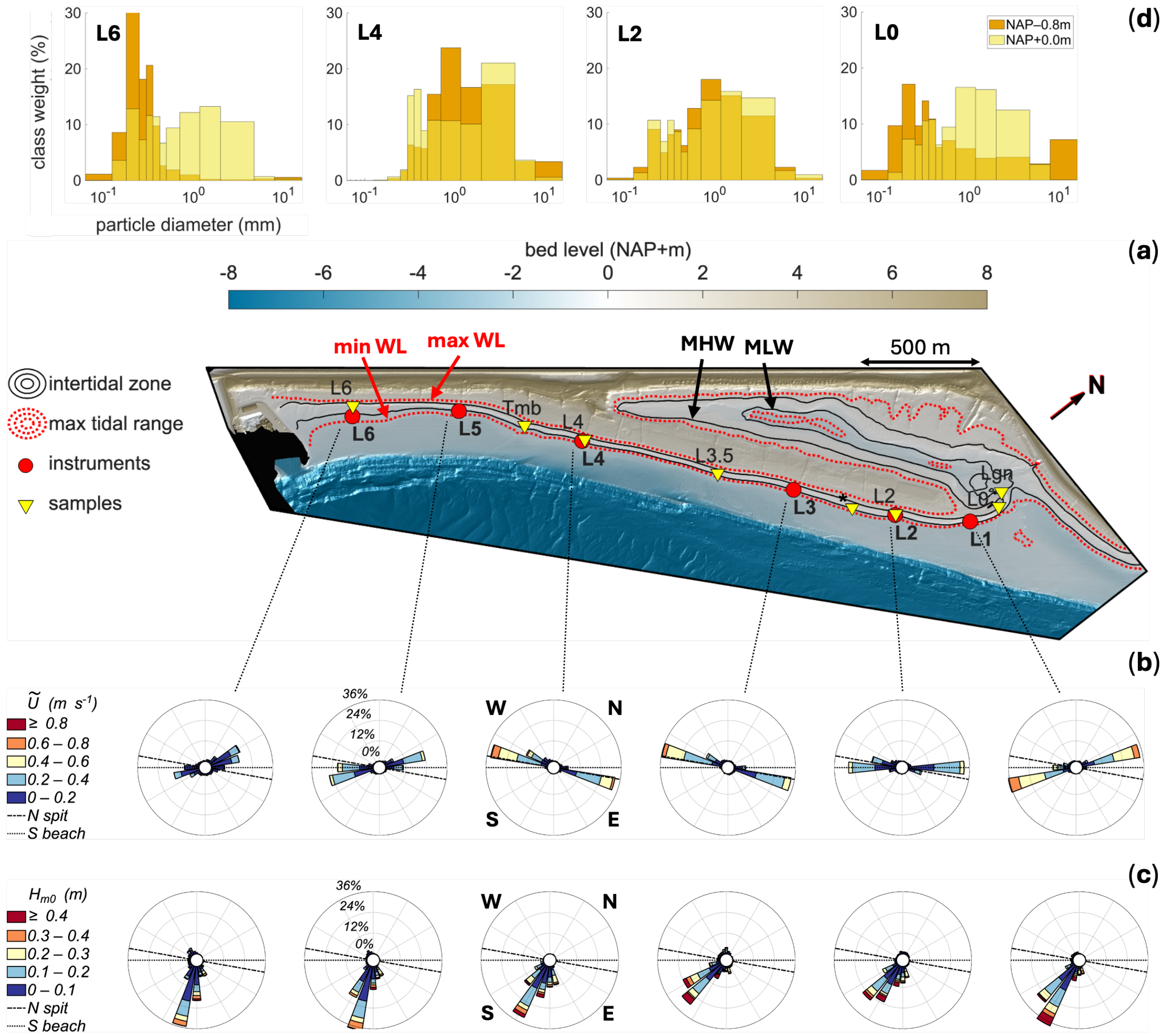

Figure 3 (**a**) DEM from 30 May 2022 (2022 Q2). Red dots are locations of velocimeters + pressure sensors at depth NAP-0.7 m. Yellow triangles are sediment sampling locations, where Tmb = tombolo, Lgn = lagoon entrance, and * = bar/runnel (sand scraper). The mean high water (MHW) and mean low water (MLW) contours are drawn as solid black lines, together demarcating the intertidal zone. Red dotted contours mark the largest measured tidal range. (**b**) Depth-average current- and (**c**) wave roses at the ADV locations. NB: Current and wave directions represent incidence angles. (**d**) Example grain size distributions of samples collected on 21 September 2021 at four longshore locations and two depths.

sorted ($1.41 \le \sigma_G < 2$; about 13% and 24%, respectively) or even well sorted ($\sigma_G < 1.41$; about 0% and 8%). σ_G was found to be a weak function of M_G at the zero isobath, with a moderate correlation ($R^2 = 0.32$) showing that σ_G improved linearly as M_G decreased. In contrast, for the lower isobath, the correlation between the two variables was virtually absent ($R^2 = 0.13$ for a linear best fit). The error bars in the σ_G line plots indicate significant temporal variability in grain size distribution at most locations.

4.3.2 Bed surface mobility

The estimated time series of BSS and the average critical values for the D_{10}, D_{50} and D_{90} grain size percentiles indicate that currents alone frequently mobilized a large part of the grain size distribution within each tidal cycle, especially during peak flow velocities, with this likelihood significantly increasing during spring tides (Fig. 7a). In contrast, waves alone appeared much less capable to mobilize sediment during calm periods (Fig. 7b), contributing only minimally to the total sediment mobilization through combined forcing (Fig. 7c). However, during the stormy period, wave-induced forcing frequently exceeded current-induced forcing, exceeding the D_{90} threshold with regularity (Fig. 7b). A comparison of the time series of current- and wave-induced BSS (Figs. 7a–b) suggests minimal modulation of the currents by wave activity, since the current magnitude seemed predominantly controlled by the lunar phase.

Shields diagrams from the six sites along the PHZ beach (L1–L6) support the initial assumption of a mixed-energy environment. The energy conditions for predicted sediment motion ranged from wave-only (wO), through wave-dominated (wD) and current-dominated (cD), to current-only (cO), with three representative cases shown in Fig. 8). The extent of no-motion (nM) conditions varied significantly across

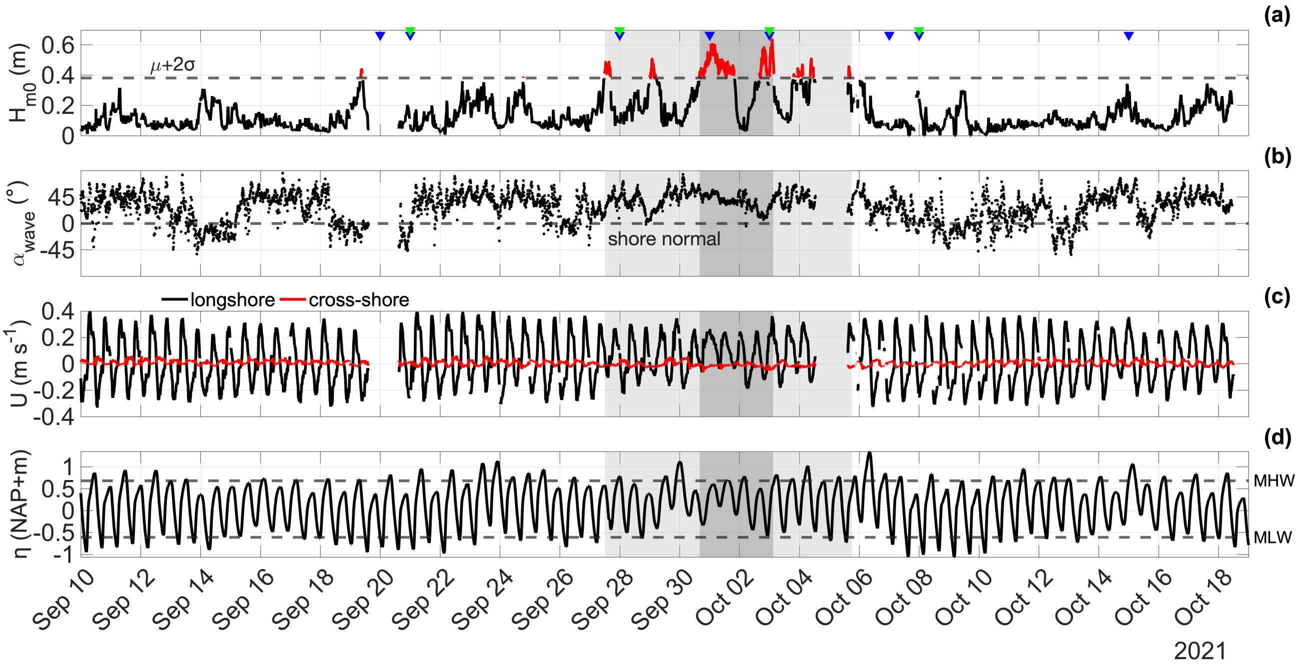

Figure 4 Nearshore hydrodynamic conditions measured on the subtidal platform at location L2 at NAP-1.4 m during the SEDMEX campaign: (**a**) significant wave height, (**b**) wave incidence angle relative to the mean shore normal (positive = from SW), (**c**) orthogonal components of the current velocity magnitude (positive = to NE or onshore) measured 0.15 m above the bed and (**d**) water surface elevation. The measurement period spans two spring-neap tidal cycles and includes a relatively energetic interval (light grey region) with peak storm waves (dark grey). Data gaps indicate periods of instrument maintenance. Downward blue and green triangles mark the timing of cross- and longshore sediment sampling surveys, respectively.

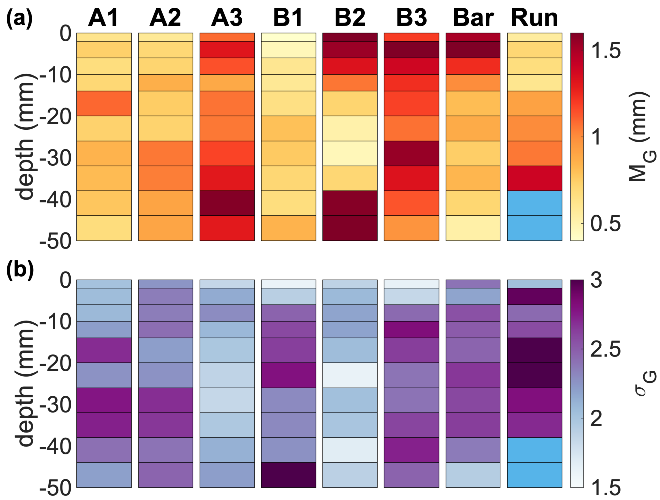

Figure 5 Vertical intravariability within bed surface samples, expressed in (**a**) M_G and (**b**) σ_G at various locations across the intertidal zone. Sample locations A1–3 (7 October 2021) and B1–3 (15 October 2021) are shown in Fig. 10a. The swash bar ('Bar' at NAP+0.4 m) and upslope runnel ('Run' at NAP+0.3 m) were sampled halfway between L2 and L3 (asterisk in Fig. 3a) on 15 October 2021. Blue areas at the bottom in 'Run' indicate reaching the groundwater.

these examples. On average, instances where currents alone mobilized the local D_{50} were less frequent (cO: 7%) compared to those driven by waves alone (wO: 15%). However, overall, current- and wave-dominated mobilization (i.e., mean cD and wD) both occurred about 11% of the time, a balance that was consistent across other grain size fractions. Nevertheless, the relative influence of waves and currents varied along the coastline, with a clear current dominance (cO+cD » wO+wD) observed at L1, and wave dominance (wO+wD » cO+cD) at L2, L3 and L6 (Fig. 8). These and more percentage values related to the hydrodynamic components are provided in Table S2 of the Supplementary Materials.

The total duration during which motion thresholds were exceeded highlights significant differences in sediment mobility potential across various grain size fractions and longshore locations. Longshore differences were striking, with much greater mobility of the entire grain size spectrum at the northeast end of the beach (70% at L1) compared to the southwest end (23% at L6). Notably, for 75% of the evaluated time, the conditions were sufficient to mobilize half of the grain sizes present (i.e., D_{50}) at location L1. Averaged alongshore, the threshold for the local D_{90} percentile was exceeded only 27% of the time, while the thresholds for the D_{50} and D_{10} percentiles were exceeded closer to 50% of the time. The coarse 2-mm grain size fraction was mobilized on average 50% of the time during the stormy period, compared to 23% of the time during the calm period. The difference was less pronounced for the fine 0.25-mm grain size fraction but remained substantial, with mobilization occurring 75% of the time during stormy conditions compared to 54% during calmer conditions. An overview of the percentage values for the full deployment, as well as for stormy and calm conditions, is given in Table S3 of the Supplementary Materials.

4.3.3 Sediment transport

The longshore variations in threshold exceedance for the different grain size fractions are also reflected in the probability density functions of net longshore bedload transport rates (e.g., Figs. 9a–b for 0.25 mm and 2.00 mm, respectively). These differences can be clearly attributed to the local BSS (Fig. 9c), but also demonstrate

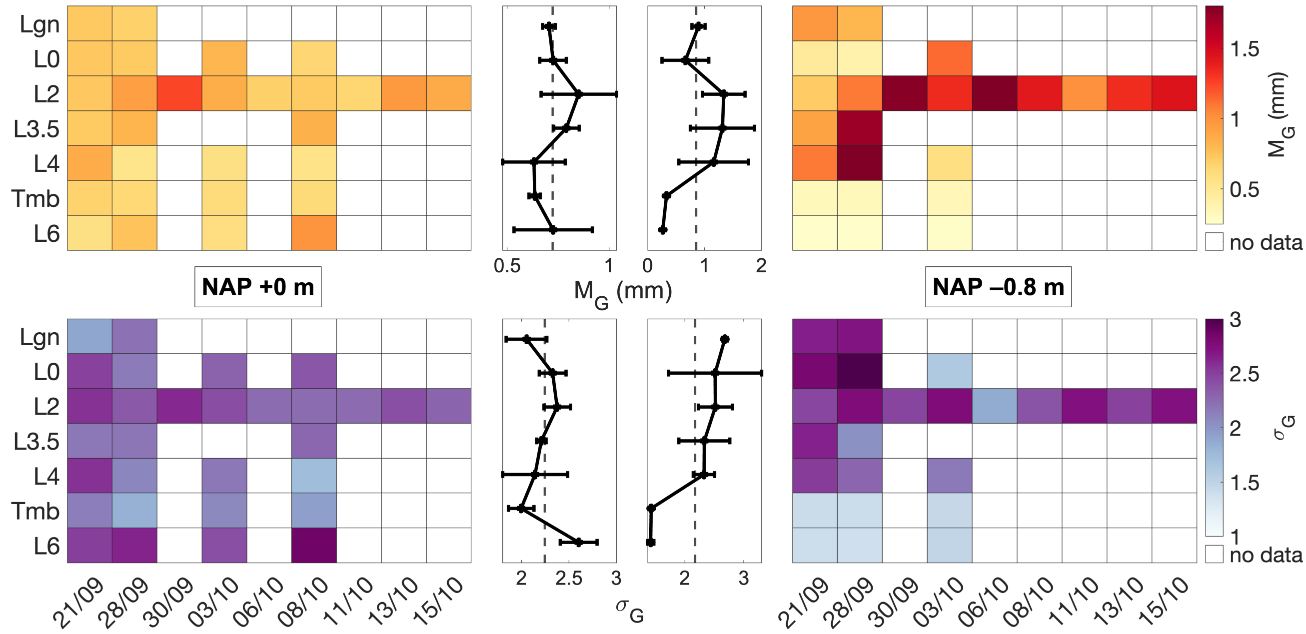

Figure 6 Temporal variability of M_G and σ_G at the seven longshore sample locations in Fig. 3a along two isobaths. Adjacent line plots and error bars indicate time-averaged longshore trends and local temporal variability. Dashed lines indicate the total longshore mean. Note the differing horizontal axis scales between the line plots.

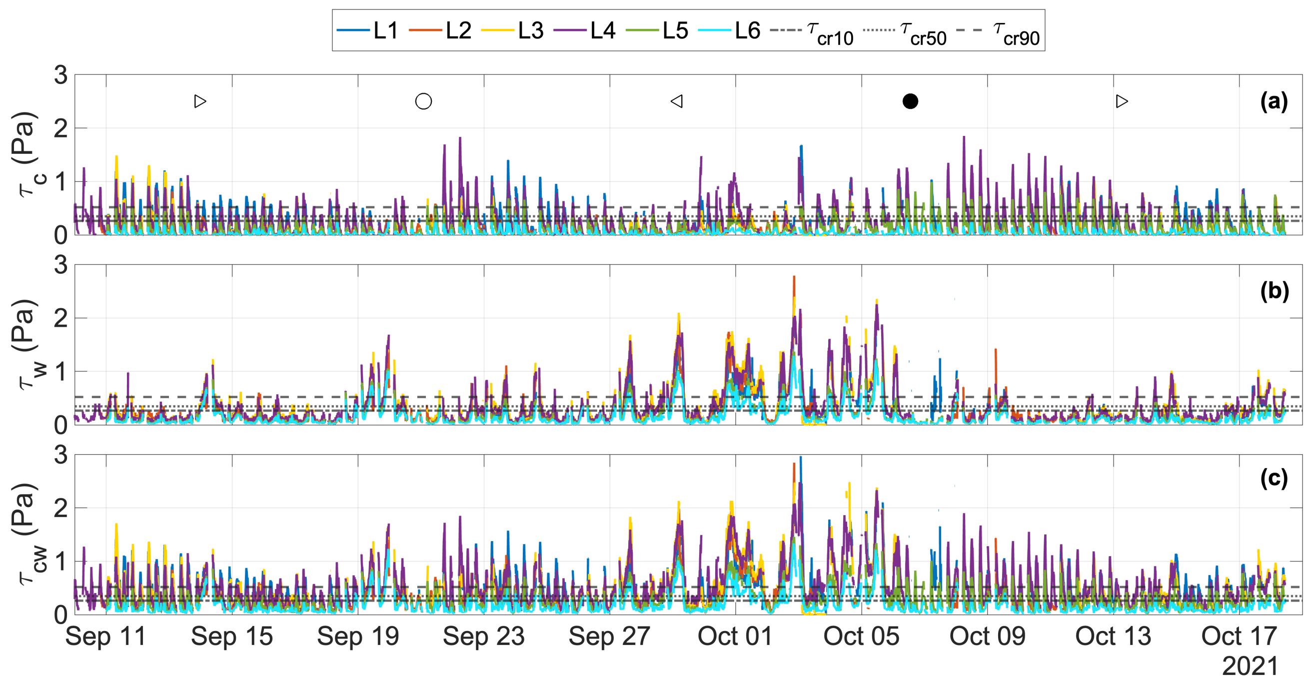

Figure 7 Time series showing (**a**) current-induced, (**b**) wave-induced and (**c**) combined current-and-wave-induced BSS at six longshore locations (L1–L6). Horizontal lines represent mean critical BSS values for three grain size percentiles (D_{10}, D_{50} and D_{90}). Upper panel symbols indicate lunar phases.

a strong dependence on the local bed surface composition. Consequently, the transport rate probabilities for the relatively coarse 2-mm fraction at location L2 are comparable to those at L1 and L4, despite L2 experiencing a significantly lower probability of high BSS values. Similarly, while L3 shows a relatively high probability of high BSS values, it also has a high probability of low transport rates, comparable to L6.

The vertical asymmetry of the curves in Fig. 9a–b implies net transport toward the northeast, corresponding to the direction of the flood current. This is consistent with the collectively positive volumes of longshore transport shown in Table 2b. The predicted gross transport volumes (per unit width) for the entire campaign reveal substantial variations in magnitude along the beach face (Table 2a), with significantly greater transport along the spit (L1–L4) compared to the south beach (L5–L6). Interestingly, while gross transport is greatest at the distal end of the spit (L1) across all grain size fractions, this is not the case for net transport (Table 2b). This disparity indicates that ebb-phase transport (negative) more effectively offsets flood-phase transport (positive) at L1 compared to other locations, highlighting the longshore variability in the relative importance of the opposite current directions.

A general trend of increasing net transport rates is ob-

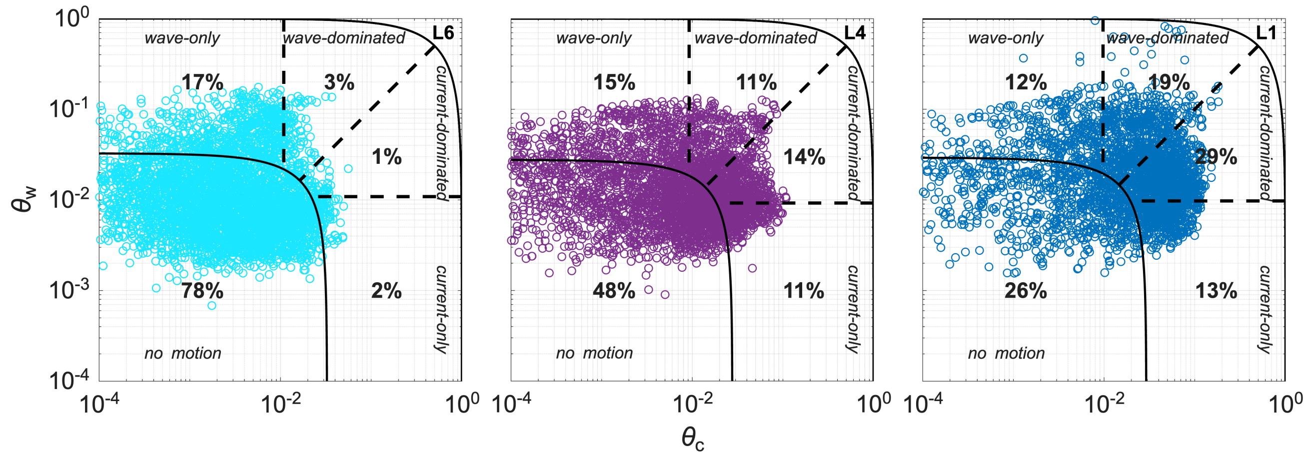

Figure 8 Wave- versus current-induced Shields number derived from measurements from three longshore locations (L6, L4 and L1, from southwest to northeast). The inner and outer solid lines demarcate the thresholds of incipient motion of the local M_G and the sheet-flow regime, respectively. Dashed lines indicate the boundaries between wave and current dominance, based on Kleinhans (2005a).

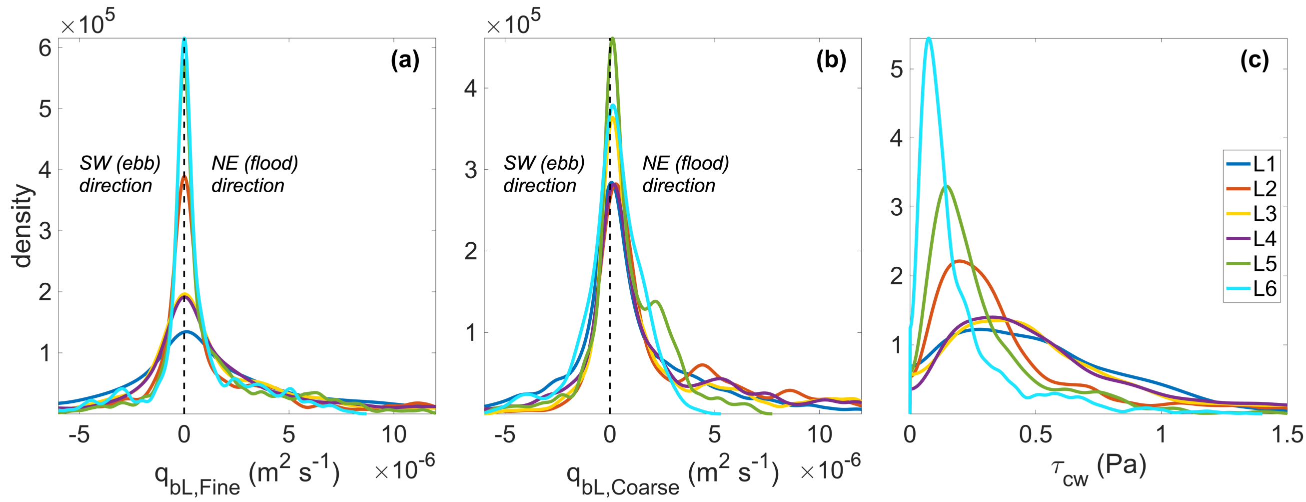

Figure 9 Kernel density estimates of net longshore bedload transport rates of the (**a**) 0.25-mm (i.e., Fine) fraction and the (**b**) 2-mm (i.e., Coarse) fraction, and (**c**) the total BSS for the six longshore locations.

served from L6 to L3 (Table 2b), resulting in a a positive transport gradient from the harbor jetty toward the halfway point along the spit. Beyond this point, transport rates are less longshore variable and show a consistent minimum at L2. However, a more consistent trend along the entire beach face is evident in the transport volume ratio of the fine to coarse grain size fraction (the last two columns in Table 2b). Except for the D_{10}/D_{90} ratio at L5, these transport volume ratios display a consistently negative but decreasing gradient from southwest (L6) to northeast (L1), suggesting that preferential transport of finer sediments becomes less pronounced along this direction.

4.4 Cross-shore grain size variability

During the field campaign, the cross-shore beach profile at L2 changed substantially (Fig. 10a). These changes were most pronounced during the stormy period between 27 September and 6 October 2021, when the profile flattened considerably by the transport of sediment from the upper part of the intertidal zone between the storm High Water (HW) and Mean Sea Level (MSL) to beneath MSL. Here, the bed level increased by up to 0.32 m, while the upper part of the beach lowered by up to 0.45 m. Throughout these morphological changes, there was substantial temporal variability in bed surface composition at nearly all eight sample locations (Fig. 10b). This variability was not simultaneous across the profile, with some locations exhibiting coarsening or fining over time and others showing improved or worsened sorting (Fig. 10c).

The time-averaged cross-shore standard deviation of low-tide M_G (σ_{M_G}) was 0.45 mm, which represented approximately 39% of the time- and spatially averaged M_G (1.14 mm). For the sorting coefficient (σ_G), the time-averaged cross-shore standard deviation (σ_{σ_G}) was 0.33, equating to about 13% of the time- and spatially averaged σ_G (2.49). Interestingly, between 28 September and 1 October 2021 — shortly following the onset of the stormy phase — the cross-shore variability in σ_G halved, while sorting slightly improved with respect to the pre-storm situation. These observations suggest that the more energetic conditions exerted a homogenizing effect on the surface sediments within this cross-shore profile, irrespective of M_G. However, the variability in M_G showed a weaker response to the time-varying wave forcing, indicating that the increased cross-shore simi-

Table 2 Estimated (**a**) gross and (**b**) net total longshore bedload transport volume ($m^3 m^{-1}$ width) per grain size percentile (excluding pores) at each of the six longshore locations over the entire field campaign. The '+' (plus) and '-' (minus) indicate longshore transport in the NE flood and SW ebb direction, respectively. The final two columns show the volume ratios of the fine to coarse (local and global) grain size fractions.

(**a**)	M_G	D_{10}	D_{50}	D_{90}	0.25	2.00	mean
L1	3.28	4.68	3.50	1.45	4.47	1.81	3.20
L2	1.47	2.35	1.48	0.74	2.49	0.95	1.58
L3	1.98	3.16	2.02	1.02	3.90	1.34	2.24
L4	1.97	3.31	2.11	0.86	3.91	1.36	2.25
L5	0.91	1.23	0.93	0.58	1.24	0.40	0.88
L6	0.54	0.77	0.56	0.26	0.71	0.23	0.51
mean	1.69	2.58	1.77	0.82	2.79	1.02	1.78

(**b**)	M_G	D_{10}	D_{50}	D_{90}	0.25	2.00	mean	$\frac{D_{10}}{D_{90}}$	$\frac{0.25}{2.00}$
L1	+1.14	+1.51	+1.20	+0.60	+1.46	+0.71	+1.10	2.53	2.05
L2	+0.97	+1.45	+0.98	+0.52	+1.52	+0.66	+1.02	2.76	2.29
L3	+1.05	+1.60	+1.07	+0.56	+1.92	+0.73	+1.16	2.87	2.64
L4	+0.88	+1.41	+0.93	+0.39	+1.64	+0.61	+0.98	3.65	2.67
L5	+0.44	+0.57	+0.45	+0.28	+0.58	+0.18	+0.42	2.09	3.18
L6	+0.07	+0.11	+0.07	+0.01	+0.10	+0.01	+0.06	8.23	10.9
mean	+0.76	+1.11	+0.78	+0.39	+1.20	+0.48	+0.79	3.69	3.95

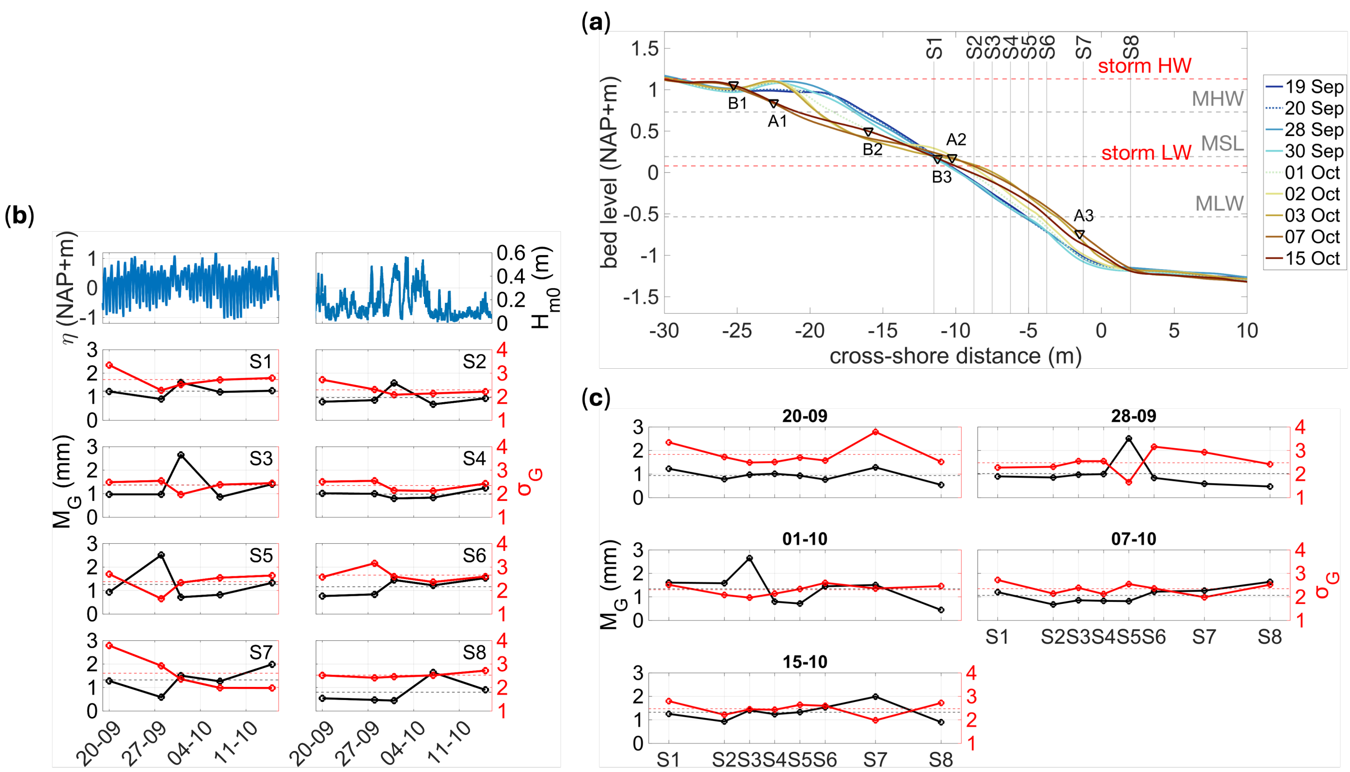

Figure 10 **a**) Fixed horizontal sampling locations (S1–8) along cross-shore transect L2 (see Fig. 3a) and bed-profile development during the period of measurement. Additional sand scraper locations are also indicated: A1–3 on 7 October 2021 and B1–3 on 15 October 2021. (**b**) Temporal evolution of bed surface composition, M_G (black) and σ_G (red), during low tide at each fixed sample location. (**c**) Spatial variability along the sample array during low tide on five different measurement days.

larity in σ_G was not necessarily accompanied by a similar trend in M_G. The cross-shore profile statistics are summarized in Table S4 of the Supplementary Materials.

To contextualize the variability observed in low-tide M_G and σ_G, it is essential to compare these metrics to their tidal variability within a single cycle. Fig. S1 in the Supplementary Materials presents time-evolution plots of M_G and σ_G, alongside concurrent measurements of water surface elevation and wave height at the eight sampling locations. Tidal fluctuations in M_G and σ_G were smallest at location S2 (0.10 mm and 0.13 mm, respectively) and reached their maximum at S7 (0.42 mm and 0.48 mm, respectively) (Fig. 11). A comparison of temporal trends in M_G and σ_G reveals evidence of covariance, as supported by some of the computed Pearson correlation coefficients. Remarkably strong covariance was observed at locations S3 (r = 0.96) and S5 (r =

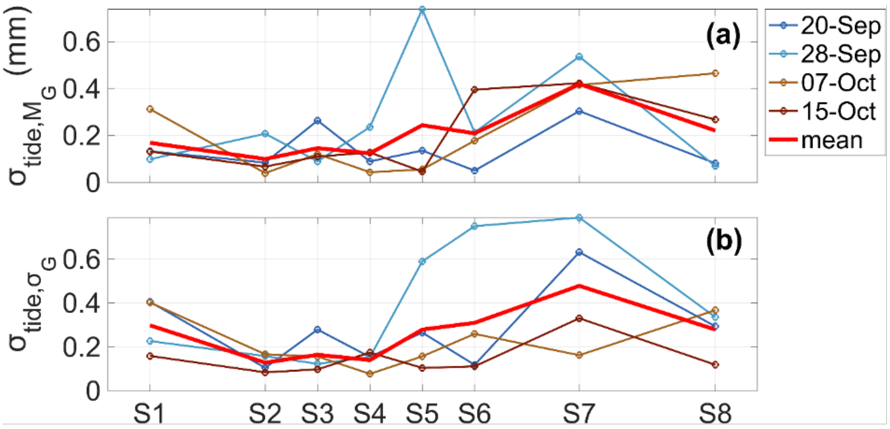

Figure 11 Tidal variation in the (**a**) mean (M_G) and (**b**) uniformity (σ_G) of the cross-shore sample array, expressed as the standard deviation at each sample location. Observations from 1 October 2021 are missing, as storm-induced elevated water levels did not allow for sampling all eight locations. The thick solid red lines represent the temporal mean standard deviation of M_G and σ_G.

0.98), which were also the only sites showing statistical significance ($p < 0.05$). The time- and spatially averaged tidal variability in M_G and σ_G were 0.20 mm and 0.26 mm, respectively (Fig. 11). This indicates that the day-to-day variability observed at low tide frequently falls within the range of tidal fluctuations occurring within a single tidal cycle. Consequently, long-term changes cannot be solely attributed to shifts in hydrodynamic or morphologic boundary conditions beyond the tide scale.

Finally, no definitive correlation was identified between changes in bed level (Δz) and bed surface composition (M_G and σ_G) across the eight sampling locations (Fig. 12). During periods of sedimentation ($\Delta z > 0$), M_G and σ_G exhibited inconsistent behavior, showing both increases and decreases without a discernible pattern. However, erosion events ($\Delta z < 0$) revealed a more distinct trend: M_G and σ_G tended to increase concurrently, as evidenced by the clustering of data points in the 2nd quadrant of Fig. 12b. This suggests that erosion generally led to coarser grain sizes and poorer sorting.

5 Discussion

The results of this study reveal considerable spatial and temporal variability in sediment composition at the artificial Prins Hendrikzanddijk beach (Figs. 6 and 10). This variability appears to be driven by the combined, and likely interacting, forces of waves and tides within this mixed-energy environment (Fig. 8). These findings emphasize the complexity of sediment transport dynamics in back-barrier beach systems, especially those characterized by poorly sorted sediment mixtures.

In contrast to open coasts dominated by waves (e.g., Huisman et al., 2016), mixed-energy conditions at sheltered coasts, such as the PHZ, are inherently more current-driven and generally much closer to the sediment motion threshold (Fig. 8). Under such conditions, a gradual winnowing of the finer sediment fractions may be expected — particularly in the presence of highly heterogeneous sediments — as the smaller particles are more frequently entrained and transported further, while updrift supply limitation prevents replenishment. This process could lead to the development of a stable deflation surface or armor layer (Hart and Plint, 1995). Such sorting processes would stabilize the surface sediments, effectively immobilizing the finer, more erodible material within the nourishment core. Consequently, the rates of sediment transport and morphologic change would be expected to gradually decline over time until a steady state is reached, in which the finest fractions are gone. However, observations from the PHZ indicate otherwise.

Despite the relatively coarse sediment mixture implemented at the nourished site, tidal currents alone were found capable of mobilizing a considerable portion of the local grain size fractions much of the time (Fig. 8). However, their contribution varies substantially along the beach and is sometimes secondary to wave action (Table S2). This indicates that morphodynamic processes shift between current-dominated, mixed-energy, and wave-dominated regimes, depending on the specific longshore location and the grain size fraction in question. Nevertheless, when averaged along the beach face, the contributions of waves and currents are roughly equal across all grain size fractions. Wave action becomes particularly dominant during stormy conditions, when waves greatly increase the mobilization of all grain size fractions (Table S3b). At certain locations, such as L6, wave action is even the sole contributor to mobilization of the coarse end of the grain size spectrum (≥ 2 mm). These periodically occurring waves are likely to play a key role in disrupting the formation of armor layers, as previously suggested in the context of wind-driven transport from the intertidal beach by Hoonhout and de Vries (2017). By contrast, at other locations, such as L1, tidal currents are sufficiently strong to also frequently mobilize coarser sediments independently. However, storm waves alone, combined with elevated water levels, can periodically alter the local bed composition by flattening the cross-shore slope and driving cross-shore sediment exchange (Fig. 10).

The high spatiotemporal variability in grain sizes observed on the PHZ beach face aligns with patterns documented on other mixed beaches (e.g., Townsend et al., 2024). At the PHZ, the pronounced horizontal heterogeneity over very short (m-scale) distances appears to

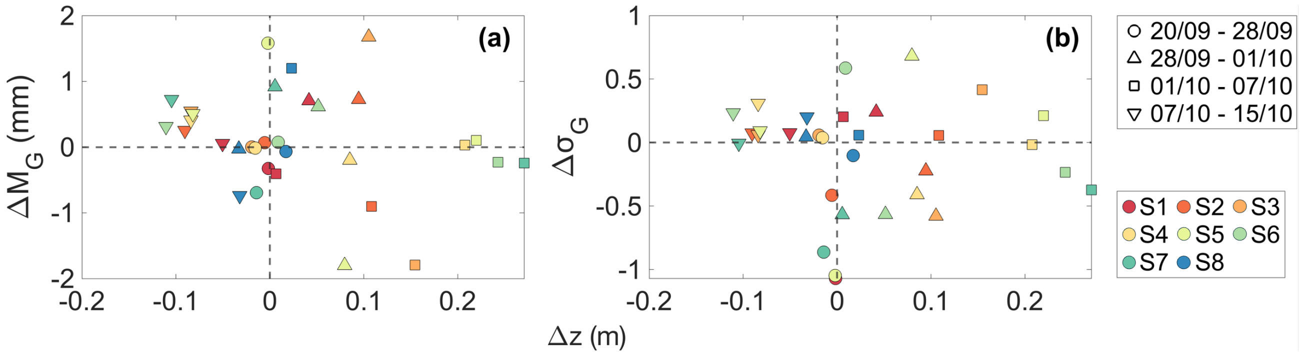

Figure 12 Temporal differences in the (**a**) mean (ΔM_G) and (**b**) uniformity ($\Delta\sigma_G$) of the surface sediments at the eight sample locations as a function of bed level change Δz in the period from 20 September through 15 October 2021. The upper legend (symbols) state the periods over which the differences were computed.

be closely linked to variations in vertical sediment layering. Sand scraper samples (Fig. 10a) revealed substantial variability in M_G and σ_G even at sub cm-scale vertical distances (Fig. 5). The observed patterns resemble to some extent swash-laminated sands (Shan et al., 2015), which typically range from mms to cms in thickness and form on the beach face as a result of swash processes. Consequently, minor surface-layer erosion can significantly alter the grain size mixture exposed at the surface, resulting in pronounced horizontal grain size differences. This phenomenon also provides insight into the relatively large sampling errors associated with the sediment sampling method employed in this study, underscoring the challenges of capturing the large-scale trends in grain size evolution. In this study, grain size metrics such as the D_{50} were used to describe sometimes polymodal sediment distributions, aligning with standard practices in sedimentology and engineering, and to facilitate the use of transport formulas. However, additional descriptors, such as modal grain sizes, could be more representative for describing (transport of) mixed sediments (Blott and Pye, 2001) and provide alternative insights in future work.

The mixed-energy hydrodynamic conditions and highly variable bed surface — maintained by ongoing erosion and deposition (Figs. 5 and 10) — are sufficient to hinder the formation of stable sorting patterns, such as a well-developed armor layer. This indicates that time alone is not enough for such features to emerge; sufficiently immobile sediment fractions relative to the forcing conditions are also required. As observed on seasonal composite beaches, the sorting — or lack thereof — on the PHZ beach face appears to be governed primarily by the intermittent transport of specific sediment fractions, driven by local hydrodynamic variability and episodic high-energy (storm) events (Table S1 and Fig. 7). A key distinction, however, may be the degree of intermittency: at the PHZ, transport of the larger portion of grain size fractions present likely occurs more frequently due to the relatively narrow range of critical motion thresholds for the sediment mixture (medium to very coarse sand), compared to those on a typical sand-gravel beach. This promotes more frequent reworking and results in more transient sorting patterns. Simultaneously, fine-grained, easily mobilized sediment fractions remain available and transport rates on the PHZ are unlikely to diminish. Meanwhile, longshore gradients in wave forcing and tidal currents (Fig. 3b–c), combined with substantial variations in bed composition (Fig. 6), will continue to drive morphologic change (Fig. 9a–b). This persistent sediment mobility suggests the PHZ has a relatively high morphodynamic activity, despite the coarse, poorly sorted nourishment material and relatively sheltered environment.

The effectiveness of implementing a coarse, poorly sorted sediment mixture and an initial armor layer is highly dependent on the local forcing conditions at the nourishment site and thus requires a site-specific, tailored approach — especially if ecological goals are also involved. Even on the relatively sheltered PHZ beach, the applied armor layer was rapidly mobilized, resulting in surface characteristics that more closely resemble the underlying sediment core. While this study does not offer definitive insights into long-term morphologic changes, the observed response to a higher-energy event — particularly changes in the cross-shore bed profile and grain sizes exposed at the surface — suggest that storm frequency and the duration of intervening calm periods may play a substantial role in the system's evolution over time. Analysis of the multi-annual evolution of the PHZ under a broad range of weather conditions and resulting hydrodynamics are needed to shed light on the effect of bed surface composition on long-term (> 5 years) morphologic adjustment.

6 Conclusions

Two years after construction of the artificial back-barrier beach, there is still significant spatiotemporal variability in its surface sediment composition. The beach is subject to diverse morphodynamic regimes due to variations in longshore wave attack and tidal current velocities. Even under calm conditions, a wide range of grain sizes can be mobilized on the beach face, with finer sediment fractions (< 0.25 mm) frequently entrained by currents, creating a near-continuous driver of preferential transport. Storm waves are required to mobilize coarse grains (> 2 mm) in certain sections of the beach, while tidal currents suffice in other areas. The absence of clear sediment sorting patterns across the beach can thus be attributed to the frequent mobilization of most grain size fractions during regular tidal cycles, with any remaining immobile fractions likely redistributed during high-energy events. Cross-shore sediment exchange also plays a crucial role in this process, as profile dynamics lead to the removal or burial of (sub)surface sediments, exposing newly mixed material and further preventing long-term sorting. Overall, the frequent mobilization of most exposed grain sizes, combined with highly heterogeneous beach sediment, ensures a constant (re)supply of unsorted material that suppresses large-scale and long-term sorting of the (sub)surface sediments. Future research on such heterogeneous beach environments would benefit from more systematic and robust sediment sampling strategies, allowing for a clearer differentiation between natural variability and measurement noise.

The Prins Hendrikzanddijk has demonstrated the potential short- to medium-term (< 5 years) effects of implementing a non-native sand mixture with coarse surface material in retrofit designs in mixed-energy environments. Rather than allowing the bed to progressively stabilize, strong tidal currents and storm waves can sufficiently remix the sediment surface layer, re-exposing fine grains and sustaining high erosion rates.

Acknowledgements

We sincerely thank all those who contributed to the SEDMEX field campaign. Special thanks go to the project staff: Marlies van der Lugt and Matthieu de Schipper; MSc students: Martijn klein Obbink, Jelle Woerdman and Roel Hoegen; technical teams of UU Earth Simulation Lab (Marcel van Maarseveen, Henk Markies, Mark Eijkelboom, Arjan van Eijk and Bas van Dam) and TU Delft (Pieter van der Gaag, Chantal Willems, Arie van der Vlies, Arno Doorn). We greatly appreciate Jan De Nul NV for supplying the high-resolution elevation data. We also acknowledge the anonymous reviewers for their constructive feedback, which significantly improved the quality of this article. Finally, we thank Maarten Kleinhans for his valuable suggestions and expertise, which have been of great value to this research.

Land Recognition

After consulting relevant resources and checking with the relevant local communities, the authors have confirmed that the lands containing their institutions and all work sites associated with this study do not have cultural or historical significance to a particular indigenous group.

Data and Codes Availability

All MATLAB scripts used for computations in the Methods section and for generating the presented figures are publicly available on GitHub (https://github.com/JornBosma/sedmex-wp2). A version snapshot of these scripts is archived on Zenodo (https://doi.org/10.5281/zenodo.14583156). Data from the SEDMEX campaign can be accessed through the 4TU.ResearchData repository (https://data.4tu.nl/collections/19c5676c-9cea-49d0-b7a3-7c627e436541).

Funding Statement

This study was conducted as part of the research program *EURECCA: Effective Upgrades and REtrofits for Coastal Climate Adaptation* (Project No. 18035), funded by the Dutch Research Council (NWO) domain Applied and Engineering Sciences.

Conflict of Interest Disclosure

The authors declare that they have no known competing interests.

Permission to Reproduce Material from Copyrighted Sources

The authors declare that no copyrighted material has been reproduced in this manuscript, except for data and processing methods detailed in the associated data paper (Van der Lugt et al., 2024), which is published under a Creative Commons Attribution 4.0 license.

Declaration on Artificial Intelligence Use

The authors declare that large language models (Writefull and ChatGPT) were used incidentally to suggest edits to text originally written by the authors. No new content was generated by these tools.

References

Arriaga, J., Ribas, F., Falqués, A., Rutten, J., and Ruessink, G. Long-term performance of mega-nourishments: Role of directional wave climate and initial geometry. *Journal of Marine Science and Engineering*, 8(12):1–21, 12 2020. doi: 10.3390/jmse8120965.

Ashida, K. and Michiue, M. Study on bed load transport rate in open channel flows. In *International Symposium on River Mechanics*, pages 1–12, Bangkok, 1973. IAHR.

Bernabeu, A. M., Medina, R., and Vidal, C. A morphological model of the beach profile integrating wave and tidal influences. *Marine Geology*, 197(1-4):95–116, 6 2003. doi: 10.1016/S0025-3227(03)00087-2.

Blackley, M. W. L. and Heathershaw, A. D. Wave and tidal-current sorting of sand on a wide surf-zone beach. *Marine Geology*, 49: 345–356, 1982.

Blott, S. J. and Pye, K. Gradistat: A grain size distribution and statistics package for the analysis of unconsolidated sediments. *Earth Surface Processes and Landforms*, 26(11):1237–1248, 10 2001. doi: 10.1002/esp.261.

Bonneville, R. Essais de synthèse des lois de début d'entraînement des sédiments sous l'action d'un courant en régime uniforme. *Bulletin du Centre de Recherche de Chatou*, 5:67–72, 1963. In French.

Brand, E. Erosion and transport of sediment and channel-shoal sediment exchange at a shoal in the Western Dutch Wadden Sea. Technical report, Utrecht University, 2016.

Buijsman, M. C. and Ridderinkhof, H. Long-term ferry-ADCP observations of tidal currents in the Marsdiep inlet. *Journal of Sea Research*, 57(4):237–256, 5 2007. doi: 10.1016/j.seares.2006.11.004.

de Schipper, M. A., de Vries, S., Ruessink, G., de Zeeuw, R. C., Rutten, J., van Gelder-Maas, C., and Stive, M. J. Initial spreading of a mega feeder nourishment: Observations of the Sand Engine pilot project. *Coastal Engineering*, 111:23–38, 5 2016. doi: 10.1016/j.coastaleng.2015.10.011.

de Schipper, M. A., Ludka, B. C., Raubenheimer, B., Luijendijk, A. P., and Schlacher, T. A. Beach nourishment has complex implications for the future of sandy shores. *Nature Reviews Earth and Environment*, 2(1):70–84, 1 2021. doi: 10.1038/s43017-020-00109-9.

de Vriend, H. J., van Koningsveld, M., Aarninkhof, S. G., de Vries, M. B., and Baptist, M. J. Sustainable hydraulic engineering through building with nature. *Journal of Hydro-Environment Research*, 9(2):159–171, 6 2015. doi: 10.1016/j.jher.2014.06.004.

Egiazaroff, I. V. Calculation of Nonuniform Sediment Concentrations. *Journal of the Hydraulics Division*, 91(4):225–247, 7 1965. doi: 10.1061/JYCEAJ.0001277.

Elias, E. P., Cleveringa, J., Buijsman, M. C., Roelvink, J. A., and Stive, M. J. Field and model data analysis of sand transport patterns in Texel Tidal inlet (the Netherlands). *Coastal Engineering*, 53 (5-6):505–529, 4 2006. doi: 10.1016/j.coastaleng.2005.11.006.

Elias, E. P., Van Der Spek, A. J., Wang, Z. B., and De Ronde, J. Morphodynamic development and sediment budget of the Dutch Wadden Sea over the last century. *Geologie en Mijnbouw/Netherlands Journal of Geosciences*, 91(3):293–310, 2012. doi: 10.1017/S0016774600000457.

Folk, R. L. and Ward, W. C. Brazos River bar [Texas]; a study in the significance of grain size parameters. *Journal of Sedimentary Research*, 27(1):3–26, 3 1957. doi: 10.1306/74D70646-2B21-11D7-8648000102C1865D.

Fordeyn, J., Lemey, E., and Perk, L. A Holistic Approach to Coastal Protection for the Prins Hendrik Polder. In *WODCON XXII*, Shanghai, China, 4 2019. https://www.researchgate.net/publication/358119462.

Grant, W. D. and Madsen, O. S. Combined wave and current interaction with a rough bottom. *Journal of Geophysical Research: Oceans*, 84(C4):1797–1808, 4 1979. doi: 10.1029/jc084ic04p01797.

Haarbosch, S. *The influence of bivalve shells, of different shapes and sizes, on current-driven sediment transport*. PhD thesis, Delft University of Technology, Delft, 2023.

Hart, B. S. and Plint, A. G. Gravelly Shoreface and Beachface Deposits. In *Sedimentary Facies Analysis*, pages 75–99. Wiley, 5 1995. doi: 10.1002/9781444304091.ch4.

Hassan, W. N. and Ribberink, J. S. Transport processes of uniform and mixed sands in oscillatory sheet flow. *Coastal Engineering*, 52(9):745–770, 9 2005. doi: 10.1016/j.coastaleng.2005.06.002.

Hayashi, T., Ozaki, and Ichibashi, T. Study on the bed load transport of sediment mixture. In *Proceedings of the Japanese Conference on Hydraulics*, volume 24, pages 35–43. Japan Society of Civil Engineers, 1980. doi: 10.2208/prohe1975.24.35.

Hegge, B., Eliot, I., and Hsu, J. Sheltered Sandy Beaches of Southwestern Australia. *Journal of Coastal Research*, 12(3):748–760, 1996.

Hoonhout, B. and de Vries, S. Field measurements on spatial variations in aeolian sediment availability at the Sand Motor mega nourishment. *Aeolian Research*, 24:93–104, 2 2017. doi: 10.1016/j.aeolia.2016.12.003.

Huisman, B. J., de Schipper, M. A., and Ruessink, B. G. Sediment sorting at the Sand Motor at storm and annual time scales. *Marine Geology*, 381:209–226, 11 2016. doi: 10.1016/J.MARGEO.2016.09.005.

Huisman, B. J., Ruessink, B. G., de Schipper, M. A., Luijendijk, A. P., and Stive, M. J. Modelling of bed sediment composition changes at the lower shoreface of the Sand Motor. *Coastal Engineering*, 132:33–49, 2 2018. doi: 10.1016/j.coastaleng.2017.11.007.

Kleinhans, M. G. Phase diagrams of bed states in steady, unsteady, oscillatory and mixed flows - Paper Q. In *In Sandpit: Sand Transport and Morphology of Offshore Sand Mining Pits*, edited by van Rijn, L. C., Soulsby, R. L., Hoekstra, P., and Davies, A. G., Los Angeles, CA, 2005a. Aqua Publications.

Kleinhans, M. G. Upstream sediment input effects on experimental dune trough scour in sediment mixtures. *Journal of Geophysical Research: Earth Surface*, 110(F4), 12 2005b. doi: 10.1029/2004JF000169.

Koninklijk Nederlands Meteorologisch Instituut. Archief code oranje & rood in 2021, https://www.knmi.nl/kennis-en-datacentrum/uitleg/archief-code-oranje-rood-in-2021.

Kroon, A., de Schipper, M., de Vries, S., and Aarninkhof, S. Subaqueous and Subaerial Beach Changes after Implementation of a Mega Nourishment in Front of a Sea Dike. *Journal of Marine Science and Engineering*, 10(8), 8 2022. doi: 10.3390/jmse10081152.

McCarron, C. J., Van Landeghem, K. J., Baas, J. H., Amoudry, L. O., and Malarkey, J. The hiding-exposure effect revisited: A method to calculate the mobility of bimodal sediment mixtures. *Marine Geology*, 410:22–31, 4 2019. doi: 10.1016/j.margeo.2018.12.001.

Nordstrom, K. F. and Jackson, N. L. Physical processes and landforms on beaches in short fetch environments in estuaries, small lakes and reservoirs: A review. *Earth-Science Reviews*, 111 (1-2):232–247, 2 2012. doi: 10.1016/j.earscirev.2011.12.004.

O'Donoghue, T. and Wright, S. Concentrations in oscillatory sheet flow for well sorted and graded sands. *Coastal Engineering*, 50 (3):117–138, 2004. doi: 10.1016/j.coastaleng.2003.09.004.

Parker, G., Klingeman, P. C., and McLean, D. G. Bedload and Size Distribution in Paved Gravel-Bed Streams. *Journal of the Hydraulics Division*, 108(4):544–571, 4 1982. doi: 10.1061/JYCEAJ.0005854.

Perk, L., van Rijn, L., Koudstaal, K., and Fordeyn, J. A rational method for the design of sand dike/dune systems at sheltered sites; Wadden Sea Coast of Texel, The Netherlands. *Journal of Marine Science and Engineering*, 7(9), 9 2019. doi: 10.3390/jmse7090324.

Ribberink, J. S. Bed-load transport for steady flows and unsteady oscillatory flows. *Coastal Engineering*, 34(1-2):59–82, 7 1998. doi: 10.1016/S0378-3839(98)00013-1.

Shan, X., Yu, X., Clift, P. D., Tan, C., Jin, L., Li, M., and Li, W. The Ground Penetrating Radar facies and architecture of a Paleo-spit from Huangqihai Lake, North China: Implications for genesis and evolution. *Sedimentary Geology*, 323:1–14, 6 2015. doi: 10.1016/j.sedgeo.2015.04.010.

Soulsby, R. *Dynamics of Marine Sands*. Thomas Telford Publications, London, United Kingdom, 1997.

Soulsby, R. L. and Clarke, S. Bed shear-stress under combined waves and currents on smooth and rough beds (TR 137). Technical report, HR Wallingford, Wallingford, 2005.

Swart, D. H. *Offshore sediment transport and equilibrium beach profiles*. PhD thesis, Delft Hydraulics Laboratory, Delft, The Netherlands, 1974, https://resolver.tudelft.nl/uuid:057cb136-5f5b-484a-878d-5616fbaeda4e. Doctoral Thesis.

Townsend, D., Leyland, J., Kassem, H., Thompson, C., and Townend, I. Exploring nearshore bed dynamics of a mixed beach using the depth of closure conceptual model. *Geomorphology*, 454, 6 2024. doi: 10.1016/j.geomorph.2024.109150.

Travers, A., Eliot, M. J., Eliot, I. G., and Jendrzejczak, M. Sheltered sandy beaches of southwestern Australia. *Geological Society, London, Special Publications*, 346(1):23–42, 1 2010. doi: 10.1144/SP346.3.

Van der Lugt, M. A., Bosma, J. W., De Schipper, M. A., Price, T. D., Van Maarseveen, M. C., Van der Gaag, P., Ruessink, G., Reniers, A. J., and Aarninkhof, S. G. Measurements of morphodynamics of a sheltered beach along the Dutch Wadden Sea. *Earth System Science Data*, 16(2):903–918, 2 2024. doi: 10.5194/essd-16-903-2024.

van IJzendoorn, C. O., Hallin, C., Cohn, N., Reniers, A. J., and De Vries, S. Novel sediment sampling method provides new insights into vertical grain size variability due to marine and aeolian beach processes. *Earth Surface Processes and Landforms*, 48(4):782–800, 3 2023. doi: 10.1002/esp.5518.

Vila-Concejo, A., Hughes, M. G., Short, A. D., and Ranasinghe, R. Estuarine shoreline processes in a dynamic low-energy system. *Ocean Dynamics*, 60(2):285–298, 4 2010. doi: 10.1007/s10236-010-0273-7.

Vila-Concejo, A., Fellowes, T. E., Gallop, S., Alejo, I., Angnuureng, D. B., Benavente, J., Bosma, J. W., Brempong, E. K., Dissanayake, P., Gazi, M. Y., González-Villanueva, R., Guimarães, R., Kennedy, D. M., Largier, J. L., van der Lugt, M. A., Montes, J., Orescanin, M., Pattiaratchi, C. B., Cajueiro Carneiro Pereira, L., Marinho da Costa Pereira, R. L., Price, T., Rahbani, M., del Río, L., Rosenthal, M., de Schipper, M., Ton, A. M., WinklerPrins, L., and Chen, Z. Morphodynamics and management challenges for beaches in modified estuaries and bays. *Cambridge Prisms: Coastal Futures*, 2:e11, 8 2024. doi: 10.1017/cft.2024.7.

Vollmer, S. and Kleinhans, M. G. Effects of particle exposure, near-bed velocity and pressure fluctuations on incipient motion of particle-size mixtures. In *River, Coastal and Estuarine Morphodynamics: RCEM 2007 - Proceedings of the 5th IAHR Symposium on River, Coastal and Estuarine Morphodynamics*, volume 1, pages 541–548, 2008. doi: 10.1201/noe0415453639-c70.

Wilcock, P. R. and Crowe, J. C. Surface-based Transport Model for Mixed-Size Sediment. *Journal of Hydraulic Engineering*, 129(2):120–128, 2 2003. doi: 10.1061/(ASCE)0733-9429(2003)129:2(120).